Breakdown and buildup mechanisms of cellulose nanocrystal suspensions under shear and upon relaxation probed by SAXS and SALS

Frédéric Pignon, Mathilde Challamel, Antoine de Geyer, Mohamad Elchamaa, Enrico Semeraro, Nicolas Hengl, Bruno Jean, Jean-Luc Putaux, Erwan Gicquel, Julien Bras, et al.

Breakdown and buildup mechanisms of cellulose nanocrystal suspensions under shear and upon relaxation probed by SAXS and SALS

Frédéric Pignon[1], Mathilde Challamel[1], Antoine De Geyer[1], Mohamad Elchamaa[1], Enrico F. Semeraro[1], Nicolas Hengl[1], Bruno Jean[2], Jean-Luc Putaux[2], Erwan Gicquel[3], Julien Bras[3], Sylvain Prevost[4], Michael Sztucki[4], Theyencheri Narayanan[4], Henda Djeridi[5]*

* Corresponding author: frederic.pignon@univ-grenoble-alpes.fr

[1]*Univ. Grenoble Alpes, CNRS, Grenoble INP (Institute of Engineering Univ. Grenoble Alpes), LRP, F-38000 Grenoble, France*

[2]*Univ. Grenoble Alpes, CNRS, CERMAV, F-38000 Grenoble, France*

[3]*Univ. Grenoble Alpes, CNRS, Grenoble INP (Institute of Engineering Univ. Grenoble Alpes), LGP2, 38000 Grenoble, France*

[4]*ESRF, The European Synchrotron, CS 40220, F-38043 Grenoble Cedex 9, France*

[5]*Univ. Grenoble Alpes, CNRS, Grenoble INP (Institute of Engineering Univ. Grenoble Alpes), LEGI, 38000 Grenoble, France*

Highlights

- The structure of CNC suspensions under shear was studied by rheo-SAXS and SALS.
- A broad range of lengthscales from nanometer to micrometer has been explored.
- Changes in cholesteric organization and disappearance of pitch under shear have been evidenced.
- The CNC organization over the three-regime rheological behavior has been clarified.
- Buildup mechanisms, from nematic to cholesteric were highlighted on large scales.

Graphical Abstract

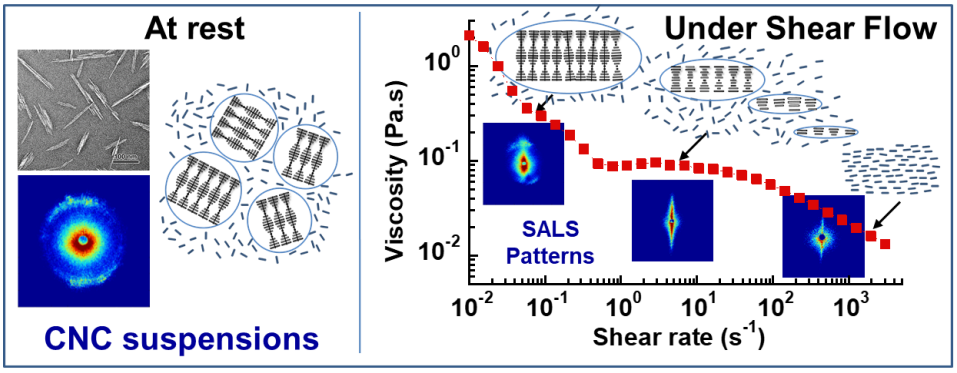

Abstract

The breakdown and buildup mechanisms in concentrated cellulose nanocrystal (CNC) suspensions under shear and during relaxation upon cessation of shear were accessed by small-angle X-ray or light scattering combined with rheometry. The dynamic structural changes over nanometer to micrometer lengthscales were related to the well-known three-regime rheological behavior. In the shear-thinning regime I, the large liquid crystalline domains were progressively fragmented into micrometer-sized tactoids, with their cholesteric axis aligned perpendicular to the flow direction. The viscosity plateau of regime II was associated to a further disruption into submicrometer-sized elongated tactoids oriented along the velocity direction. At high shear rate,

regime III corresponded to the parallel flow of individual CNCs along the velocity direction. Upon cessation of flow, the relaxation process occurred through a three-step buildup mechanisms: i) a fast reassembling of the individual CNCs into a nematic-like organization established up to micrometer lengthscales, ii) a slower formation of oriented large cholesteric domains, and iii) their isotropic redistribution.

Keywords: Cellulose nanocrystals, rheo-SAXS, SALS, shear-flow, cholesteric phase, structural organization.

1. Introduction

Cellulose nanocrystals (CNCs) are particularly attractive crystalline nanoparticles for the design of new bio-based materials with enhanced mechanical, optical or barrier properties. These nanocelluloses display outstanding mechanical properties, such as shear modulus as high as 120-150 GPa and strength up to 6 GPa for CNCs (Eichhorn et al., 2005) together with high aspect ratio and low density, in addition to their biodegradability, non-toxicity and biocompatibility (Siquieira et al., 2010; Dufresne et al., 2017). The knowledge of the flow-induced structures in aqueous CNC suspensions is crucial in their processing to bio-based materials with better performance and controlled structural organization (Thomas et al., 2018). Moreover, understanding the complex rheological behavior observed in these suspensions is of primary interest in the field of biorefinery. More specifically, controlling the dynamic orientation of CNCs under flow has a direct consequence on the macroscopic optical and mechanical properties of the material (Siquieira et al., 2010; Dufresne et al., 2017; Kargarzadeh et al., 2018) and potential industrial applications (Domingues et al., 2014; Tang et al., 2017). In order to improve the development of nanocellulose-based materials, several processes involving shear flow or pressure forces have been subject of *in*

situ structural investigations. For example, time-resolved *in situ* small-angle X-ray scattering (SAXS) was successfully employed to access the structural organization and growth of accumulated particles near the membrane surface during cross-flow ultrafiltration (Jin et al., 2015; Rey et al., 2019; Semeraro et al 2020). *In situ* and real time grazing-incidence wide-angle X-ray scattering (GIWAXS) was used to investigate the influence of suspension concentration, shear-cast velocity, and drying temperature on the ordering of the CNCs during the casting process (Sanchez-Botero et al., 2018). To develop these processing methodologies and understand the effect of shear flow on the structural arrangement in CNC suspensions, more fundamental approaches are required.

In the literature, the structural organization in CNC suspensions at rest and their phase diagram have been well characterized. CNC suspensions are known to exhibit a phase separation behavior with coexisting isotropic and liquid-crystalline phases (Revol et al., 1992; Dong et al., 1996; Orts et al., 1998; Ebeling et al., 1999; Schütz et al., 2015; Urena-Benavides et al., 2011; Lagerwall et al., 2014; Lenfant et al., 2017; Gicquel et al., 2019; Xu et al., 2020). At rest, these two phases macroscopically separate over time since the liquid-crystalline phase has a higher density. This lower phase, referred to as the chiral nematic or cholesteric phase, is characterized by a long-range orientational order of the CNCs combined with a helical modulation of their director (local alignment) (Lagerwall et al., 2014; Mitov, 2012). Before complete phase separation, the cholesteric phase exists as microdomains, or tactoids, in the isotropic phase (Wang et al., 2016; Wang and MacLachlan 2018; Tran et al., 2018; Liu et al., 2019). The phase diagram is characterized by two critical concentrations, C_i, and C_a. Below C_i, the suspension is fully isotropic and above C_a it is fully anisotropic (cholesteric). The coexistence region lies between these two values. The structural features of this phase separation have been investigated by different techniques. Firstly, at

nanometric lengthscales, SAXS and small-angle neutron scattering (SANS) measurements have allowed the determination of the evolution of the interparticle distance, *d*, between CNCs as a function of concentration. Secondly, at micrometric scale, polarized light optical microscopy was used to determine the phase diagram and measure the helical pitch, *P*, as a function of volume fraction (Revol et al., 1992; Bercea and Navard 2000; Dong et al., 1996, Urena-Benavides et al., 2011). *P* corresponds to the distance needed for a 360° rotation of the director, which can also be obtained from laser diffraction experiments (Schütz et al., 2015). These results have shown that both *d* and *P* decrease with increasing concentration.

The rheological behavior of CNC suspensions under shear and at intermediate concentrations, corresponding to the co-existence of isotropic and cholesteric phases, displays the well-known three-region behavior typical of liquid crystalline systems, characterized by a shear-thinning region followed by plateau region and then a second shear-thinning region (Onogi and Asada, 1980). Aiming at understanding this complex rheological behavior, some previous studies focused on characterizing the organization of CNCs under shear. First, at nanometer lengthscales, for example by rheo-SANS (Orts et al., 1998; Haywood et al., 2017) or rheo-SAXS (Ebeling et al., 1999), and second at micrometric lengthscales by polarized light optical microscopy (Bercea and Navard 2000; Shafiei-Sabet et al., 2012; 2014; Derakhshandeh et al., 2013), as well as rheo-SALS (small-angle light scattering) (Xu et al., 2017; Qi et al., 2019) and single droplet oscillatory platform with fluorescence and polarized light optical microscopy (Alizadehgiashi et al., 2018). These results enabled structural interpretation of the three-domain regime. The first region of shear thinning has been attributed to a progressive disruption of large chiral nematic domains into smaller ones. The plateau region corresponds to the increasing alignment of these small chiral domains along the flow direction with their helical axis orienting perpendicular to the velocity direction. Finally, the second

region of shear thinning at the highest shear rates corresponds to the disruption of all these cholesteric domains, releasing all CNCs that, in turn, could be individually oriented along the flow direction. Nevertheless, until now, only few results have been obtained at the micrometer scale, which would be the relevant lengthscale to follow the evolution of the cholesteric organization under shear. Polarized light optical observations under shear (Shafiei-Sabet al., 2012; Derakhshandeh et al., 2013; Shafiei-Sabet et al., 2014) have shown the breakdown and alignment of chiral nematic domains pertaining to the three-region behavior, and rheo-SALS data have revealed the shear-induced breakup of the CNCs above a critical shear rate (Xu et al., 2017) or under different pH conditions (Qi et al., 2019). Studying film formation by polarized light microscopy upon drying of CNC suspensions, Gray and Mu (Gray and Mu, 2019) attempted to decouple changes in texture due to evaporation from those due to shear relaxation for a sample in which gelation occurred before it reached the iridescence pitch values. These authors observed a transitory nematic-like texture that was induced by shear during the preparation of the sample for polarized light microscopy. They proposed that the transition between chiral nematic and nematic structures involved a twist-bend-like intermediate and not an untwisting of the chiral nematic phase (Gray and Mu, 2016). From polarized light optical and scanning electron microscopy images, Park et al. (2014) have shown that a better control of the helix orientation was achieved in films of dried CNCs by subjecting the suspension to a circular shear flow during drying. This induced the deformation of tactoids into ellipsoids, thereby breaking the symmetry in such a way that a vertical helix orientation became favored.

Despite all these recent advances on the monitoring of the organization of CNC suspensions, until now, no *in situ* characterization of the pitch evolution at the micrometric lengthscale as a function of the shear flow has been carried out. In this work, in order to obtain a complete structural

interpretation of this complex three-regime flow curve, the mechanical response under flow (viscosity as a function of shear rate) has been correlated to structural observations at different lengthscales: from the nanometer scale of the CNCs to the micrometer scale corresponding to their organization into a chiral nematic liquid-crystalline phase.

New features of the organization of CNCs at micrometer lengthscales were evidenced thanks to dedicated channel-type quartz flow cells combined with a 2D-SALS set-up (Piau et al., 1999). Specifically and unambiguously, this allowed characterizing the evolution of the pitch distance and its appearance or disappearance as a function of time and applied shear rate both under flow and upon its cessation. Furthermore, a combined rheology and small-angle X-ray scattering (rheo-SAXS) setup available at the European Synchrotron Radiation Facility (ID02 TRUSAXS beamline) allowed an *in situ* and time-resolved study of the CNC orientations and structural properties at nanometer scales in the dispersions under flow. More specifically, new aspects have been evidenced thanks to measurements performed in radial and tangential modes of observation.

From *in situ* SALS and SAXS measurements, a straightforward analysis of the 2D-patterns with azimuthal, sector or annular average of the scattering intensities over a broad q-range allowed to deduce the time dependent evolutions of three important parameters: the anisotropy parameter, the mean orientation direction of flowing objects, and the pitch value, P as well as its presence or disappearance. Correlated with the changes in viscosity measurements, the evolution of these three parameters as a function of shear rate and time enabled a consistent description of the breakdown and buildup mechanisms of the structural organization of CNCs from nanometer to micrometer lengthscales. The dynamic changes of liquid crystalline microdomains, or tactoids, and their chiral nematic organization under shear flow were then related to the well-known three-regime behavior, as well as during the relaxation after cessation of shear.

2. Materials and Methods

2.1. Cellulose Nanocrystals

Cellulose nanocrystals (CNCs) were purchased from UMaine Development Center (University of Maine, USA) as an aqueous suspension with a stock concentration of C = 12.2 wt%. A series of samples at different concentrations were prepared by dilution in deionized water followed by 2 h of vigorous stirring of the suspensions. NaCl was added to reach a fixed ionic strength of 10^{-2} mol L^{-1}. These suspensions were then sonicated using a sonication probe (Branson Digital sonifier) and applying at least 2 kJ per gram of CNCs.

2.2. Rheo-SAXS

All X-ray scattering measurements were performed at the ID02 beamline at the European Synchrotron Radiation Facility (ESRF), Grenoble, France (Narayanan et al., 2018). The wavelength of incident X-rays was λ = 0.995 Å and two sample-to-detector distances D (2 and 10 m) were used. SAXS measurements covered the range of scattering vector magnitude: 8×10^{-3} $nm^{-1} \leq q \leq 5$ nm^{-1}, where $q = (4\pi/\lambda) \sin(\theta/2)$ with θ the scattering angle. The corresponding nominal lengthscale ($\sim 2\pi/q$) range is 1.25 nm $\leq l \leq$ 785 nm. Combined rheometric and SAXS measurements were carried out using the Rheo-SAXS set-up available at the ESRF (Panine et al., 2003). The setup consisted of a Haake Rheo-Stress RS6000 stress-controlled rheometer, and homemade polycarbonate Couette-type shear cells with internal diameter ID = 20 mm, outer diameter OD = 21.5 mm, and height = 50 mm. The bottom gap was 0.6 mm in order to avoid any artefact from boundary conditions. The temperature was set to 25 °C with a stability of 0.1 °C. Both radial and tangential positions were used to access different observation planes and allowed discriminating a

uniaxial or probable biaxial CNC orientation. The incident X-ray beam crossed through either the center of the cell along the radial direction (Ra) (perpendicular to the velocity/vorticity plane) or the center of the gap along the tangential direction (Ta) (perpendicular to vorticity/shear gradient plane) where *v* is the velocity and grad *v* is the velocity gradient (Panine et al., 2003). In the radial configuration (Ra), the beam was parallel to the velocity gradient (*grad v*), and the (*z*, *v*) plane was probed. In the tangential position (Ta), the beam was parallel to the velocity direction (*v*), and the (*z*, *grad v*) plane was probed as shown in **Fig. 1**. For this reason, the beam size was collimated to 0.3 mm × 0.15 mm in the vertical and horizontal directions, respectively. Measured scattering patterns were normalized to an absolute intensity scale after applying standard detector corrections and subsequently azimuthally averaged to yield I(q), or sector averaged in vertical z direction, to yield $I_v(q)$. Before the shear flow experiments with CNC suspensions, the Couette-type shear-cell was filled with demineralized water (Milli-Q) and the normalized background scattering of the cell was registered. This background scattering of the cell filled with water was subtracted from the normalized scattering patterns of the CNC suspensions in all shear flow experiments. For static sample characterization, a temperature-controlled flow-through capillary cell (inner diameter = 1.95 mm) was used to measure the absolute scattered intensity of dispersions at rest at T = 22 °C. It allowed measuring sample and background scattering at the same position of the capillary, thereby allowing a very reliable subtraction.

2.3. SALS under Shear Flow

The light scattering set-up used for the experiment was developed and built as described elsewhere and schematically shown in **Fig. 2** (Piau et al., 1999). It consists of a 2 mW laser beam (He-Ne) with a wavelength of 632.8 nm and a Fresnel lens for collection of the forward scattered

light. The detector was an Allied Vision (AV MAKO G-419B POE) monochrome digital camera: CMOS sensor (2048 × 2048 pixels, 11.3 × 11.3 mm^2). Image processing was performed with a video system and specifically developed software (Vimba Matlab) that allowed regrouping and averaging of scattering intensity with SAXS Utilities software (Sztucki and Narayanan 2007). The scattering patterns were recorded by the camera and video system throughout the experiment. The modulus of the scattering vector is given by $q = [(4\pi/\lambda) \sin(\theta/2)]$, where λ is the wavelength of the light in the sample and θ the scattering angle. The light scattering measurements covered a q-range from 2×10^{-4} to 4×10^{-3} nm^{-1}. The shear flow cell consisted of a rectangular quartz glass cell (height H = 1 mm, width W = 7.4 mm, and length L = 10 mm) as depicted in **Fig. 2** (these two dimensions have been chosen to fit with usual convention, although the channel in this case is positioned vertically (with the longer dimension in vertical direction) contrary to the usual usage for example in microscopy observations where the channel is positioned horizontally.

The shear flow cell was coupled with a syringe pump to vary the flow rate Q and thus the shear rate inside the channel. For high aspect ratio H/W << 1 which is the case here H/W = 0.135, the mean shear rate $\dot{\gamma}_y$ in the rectangular channel was calculated using the following equation (Son, 2007).

$$\dot{\gamma}_y = \frac{6Q}{WH^2} \qquad \textbf{(Eq. 1)}$$

To evaluate the variation of shear rate inside the channel in the x direction along the laser beam propagation, in the thickness H of the sample, calculations were performed (**Fig. S1**) from (Son, 2007) of the apparent shear rate $\dot{\gamma}_a$ of a rectangular die and the wall shear rate $\dot{\gamma}_w$ that took into account the shear thinning behavior (and corresponding shear thinning index n for each regimes of flow). This values of shear thinning index n were deduced from our previous results (Gicquel et al., 2019). One can see that for regimes II and III, the differences are negligible for the three

calculated shear rates ($\dot{\gamma}_y$, $\dot{\gamma}_a$, $\dot{\gamma}_w$) and that for regime I the wall shear rate $\dot{\gamma}_w$which is higher for each flow rate applied in regime I, stay in the limits of the regime I for the exploited results in this work.

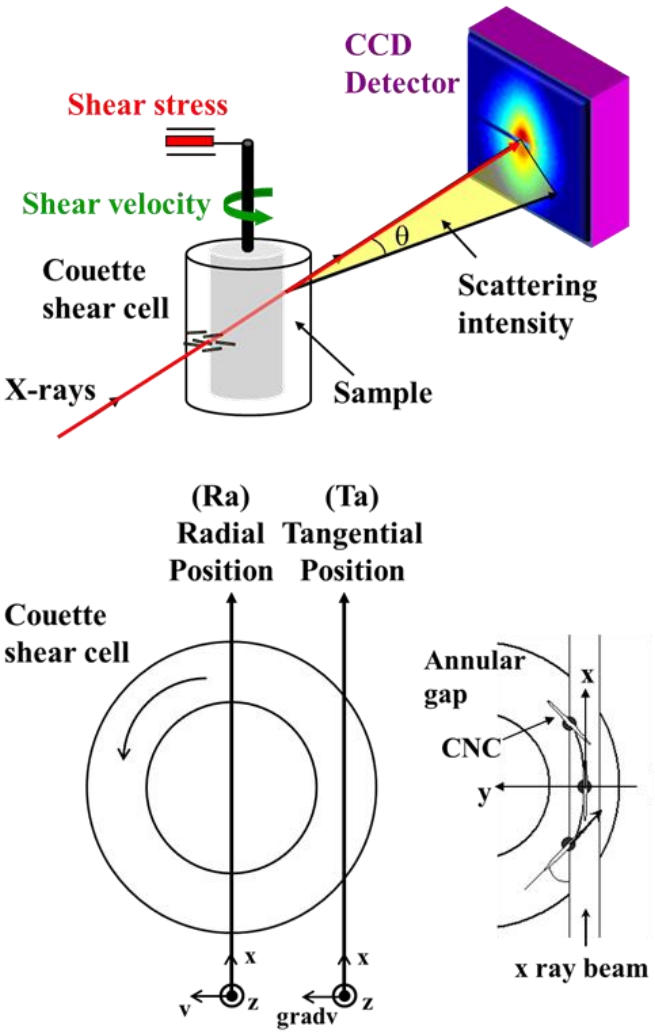

Figure 1. Rheo-SAXS setup and observation planes related to radial or tangential beam position.

The flow rate *Q* values ranged from 1 µL min^{-1} up to ≅150000 µL min^{-1} (0.01 s^{-1} to 2027 s^{-1}).

During the experiments, the laser beam was directed perpendicular to the walls of the flow cell, along the *x*-direction and is positioned in middle of the channel (*z* = 3.5 mm), through the sample

that scattered on the Fresnel lens. The scattering intensity collected by the Fresnel lens was then focused towards the camera and recorded. The azimuthal averages of the scattering intensities were calculated using the SAXS Utilities software. In order to establish the magnitude of anisotropy in the vertical and horizontal directions, scattering along the vertical (I_z) and horizontal (I_y) axes were extracted by integrating the scattering intensity over a sector of 20° around the vertical (z) and horizontal (y) axes, respectively. Two anisotropic degrees, I_v and I_h, were defined as the mean value of I_z and I_y in the q-range (1.344–1.656) × 10^{-3} nm^{-1}. From these integrations the mean anisotropy parameter was defined (Pignon et al., 2009):

Anisotropy SALS = abs $((I_v - I_h)/(I_v + I_h))$ **(Eq. 2)**.

Annular averages were also calculated over q range from (2.10^{-3} to 4.10^{-3}) nm^{-1} , to define the scattering intensity as a function of the ψ azimuthal scattering angle in the plane of the 2D SALS patterns, in order to quantify the degree of orientation as well as the angular variation of this degree of orientation. It allowed following the maximum intensity of the q_P representative of the direction of the helical axis of the cholesteric organization, or the orientation of the oval shaped SALS patterns, related to the orientation of the nematic like tactoids, as well as the relaxation features. Consequently, this set-up allowed accessing the orientation and structural changes in each CNC suspension, as well as the pitch distance evolution, under flow or relaxation, as a function of time and shear rate $\dot{\gamma}_y$.

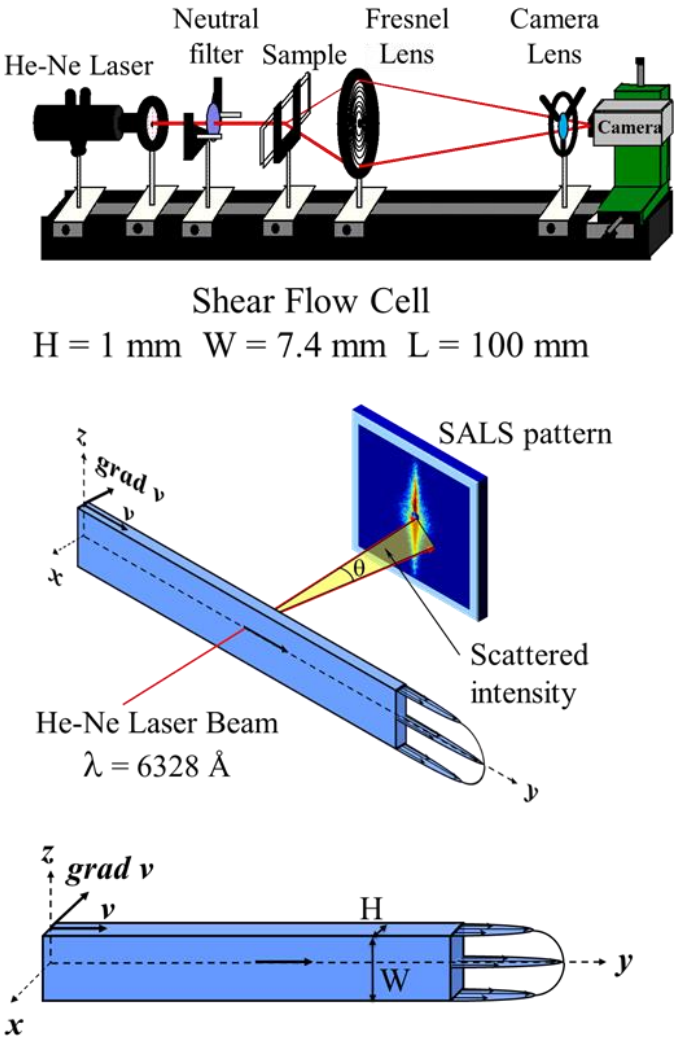

Figure 2. Schematic description of the SALS under shear flow setup.

2.4. Rheometric Measurements

Rheometric measurements were carried out using a shear rate controlled rheometer (DHR3, TA Instrument) with a cone–plate geometry of 65 mm diameter and angle of 2° in the same conditions as in scattering experiments. These values of shear thinning index *n* were deduced from our previous results (Gicquel et al., 2019; Rey et al., 2019). Measurements were performed at a fixed temperature of 25 ± 1 °C. An evaporation-proof system has been added on the top of the geometry to ensure the saturation of the atmosphere of the sample. Direct observations of the shear profile at

the outer edge of the rheometer tools, confirmed that slip did not occur and that the samples were sheared uniformly without any localization phenomena.

2.5. Transmission Electron Microscopy (TEM)

Droplets of dilute CNC aqueous suspensions were deposited onto glow-discharged carbon-coated copper grids and negatively stained with 2 wt% uranyl acetate. The specimens were observed with a JEOL JEM-2100-Plus microscope operating at an accelerating voltage of 200 kV. Images were recorded with a Gatan Rio 16 camera.

3. Results and Discussions

3.1. Structure of CNC Suspensions at Rest and Phase Diagram

The morphology of the CNCs considered in this work and their phase diagram in aqueous suspension have been studied in detail in previous publications (Gicquel et al., 2019; Semeraro et al., 2020). SAXS data from diluted suspensions at rest, assuming a parallelepipedal shape for the sonicated CNCs, gave 121 × 20 × 5 nm^3 average dimensions. The TEM images showed individual acicular particles constituted of a few laterally-associated rodlike crystallites as presented in **Fig. S2** (Gicquel et al., 2019). From previous polarized light optical observation of several suspensions at rest (Gicquel et al., 2019), three regions and two critical concentrations were described in the phase diagram. The first critical concentration, C_i, defined the beginning of the biphasic regime and had a value C_i ~ 7.5 wt% (ϕ_i = 4.82 vol%) and the second critical concentration, C_a, corresponded to the onset of the fully anisotropic phase with C_a ~ 13.3 wt % (ϕ_a = 8.75 vol%). Below C_i, only the isotropic phase was present in the whole sample. The biphasic domain extended from C_i to C_a. In this intermediate domain, the volume fraction of the liquid-crystalline phase

increased according to the regular increase of the chiral nematic domain. Above C_a, the anisotropic phase occupies the whole volume of the sample.

Figure 3a shows the azimuthally-averaged scattering intensity, $I(q)$, of CNC suspensions plotted over a broad q-range combining SAXS and SALS data of suspensions at rest. The mean interparticle distance d as well as the phase diagram of these sonicated CNC suspensions as a function of CNC concentration have previously been studied (Gicquel et al., 2019; Semeraro et al., 2020). The mean interparticle distance between the elementary CNCs has been deduced from the scattering intensities of CNC suspensions probed by SAXS. $I(q)$ *vs* q plots of the SAXS data revealed a maximum of intensity at a position q_{peak} for each CNC concentration (Rey et al., 1999). The mean interparticle distance d was then calculated from $d=2\pi/q_{peak}$ and plotted as a function of concentration in **Fig. 3b**. As shown in the previous work (Gicquel et al., 2019) the power law fits of the $d(C)$ evolution yielded a $d \propto C^{-1/2}$ scaling behavior, which is characteristic of long cylinders or rod-like colloids in a nematic arrangement. Time resolved SAXS performed on a levitating CNC drop have revealed structure evolutions of CNC dispersions during evaporation (Liu et al., 2019). Scaling analysis of the concentration dependence of the separation distance suggested that assembly of CNC can be divided into three regions as a function of the concentration with power law exponents ranging from −1/3 to −1 with increasing concentration. Comparing the concentration dependence of the interparticle distance measured in sealed capillaries, good agreement was found for the scaling behavior, $d \propto C^{-1/2}$ for volume fractions between 2 and 6 vol % characteristic for the biphasic state of CNC dispersions.

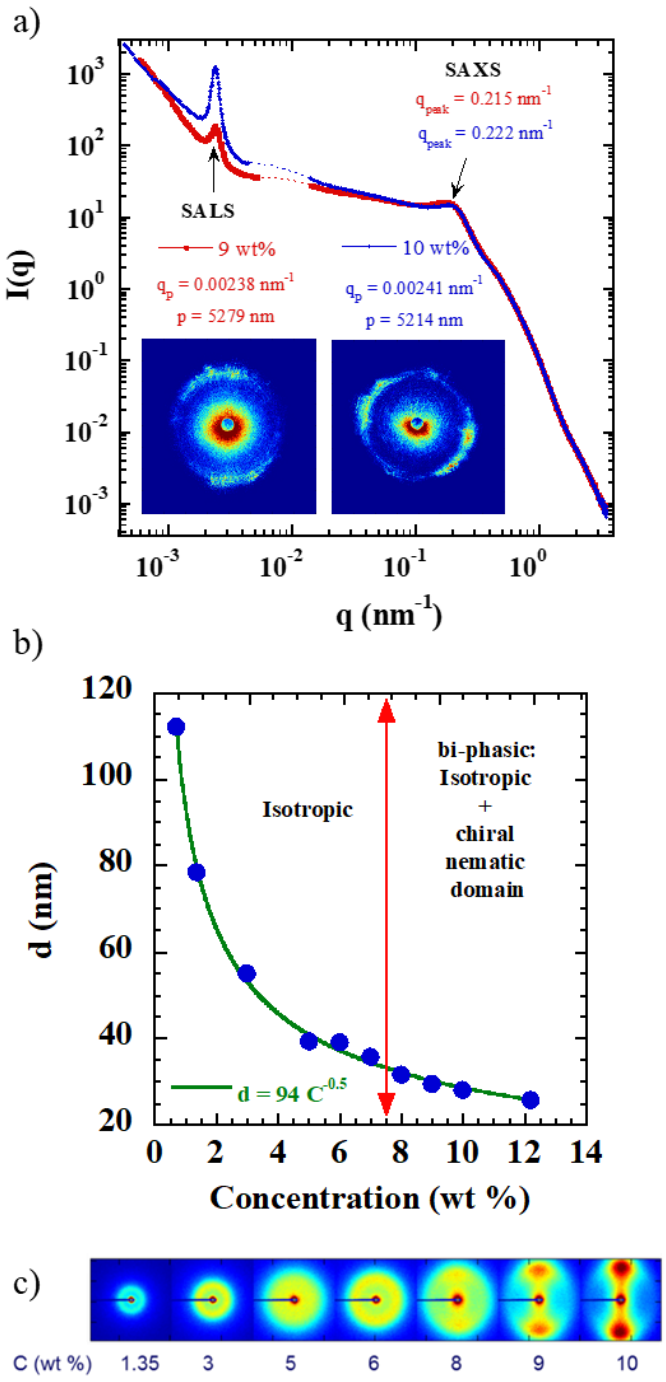

Figure 3. Scattered intensity versus *q* plots from SAXS and SALS data of 9 and 10 wt% CNC suspensions at rest a) concentration dependence of the interparticle distance, *d* of CNC suspensions at rest. Pitch values, *P*, in (a) were deduced from the q_P position in the SALS pattern and interparticle distance, *d* in (b) were deduced from the q_{peak} position observed in the SAXS pattern in (c).

SALS measurements of suspensions at rest allowed characterizing the pitch of the cholesteric phase for two CNC concentrations. The SALS patterns of suspensions at rest revealed a ring corresponding to a particular distance in the sample as presented in **Fig. S3**. As described in several previous analyses (Schütz et al., 2015; Frka-Petesic et al., 2017; Liu et al., 2019), this ring was attributed to the half-pitch of the cholesteric phase. The pitch values P, were calculated from the q_P position in the SALS patterns using $P = 4\pi/q_P$, giving P = 5279 and 5214 nm for CNC suspensions at 9 wt% (ϕ = 5.82 vol%) and 10 wt% (ϕ = 6.49 vol%) respectively.

3.2. Procedures to Monitor Breakdown and Buildup Mechanisms

Three procedures have been used to characterize the changes in structural organization under shear or to follow relaxation processes. In the first procedure (P1), the CNC suspension was injected in the canal at a large Q of 79 L min^{-1} corresponding to a shear rate of 1068 s^{-1}. Then the suspension was kept at rest for 2 to 3 h (rest step), until the cholesteric organization was recovered. This was checked by monitoring the SALS patterns, which showed an isotropic diffuse scattering (random orientation of the cholesteric phase in the canal) alongside a ring-like pattern related to the presence of the pitch (**Fig. S3**). This rest step ensured that all the subsequent measurements were starting from the same initial conditions, with no specific orientation and an anisotropic phase volume fraction at its equilibrium value. Then, a specific constant shear rate (flow rate Q) was applied and a series of SALS patterns were recorded to follow the transient state of the structural organization as a function of time, up to reaching the corresponding steady state (stabilization of SALS patterns). This P1 procedure was then performed at three shear rates corresponding to the middle of regimes I, II and III. The second (P2) and third (P3) procedures were identical to P1 until the rest step. Then, for P2, the shear rate was increased step by step, waiting for stabilization of the

SALS pattern prior to applying the next shear rate value. Instead, in P3, a high shear rate was applied until the stable state was reached, then the syringe pump was stopped and SALS patterns were acquired to follow the relaxation of the structural organization as a function of time.

3.3. Break-down Mechanisms of CNC Suspensions under Shear

3.3.1. Rheological Behavior in Steady-state

First, rheometric measurements in cone-plate geometry were performed in order to assess the typical three-regime behavior of these CNC suspensions. The steady-state shear viscosity as a function of the shear rate applied has been obtained for different CNC concentrations within the co-existence region of the phase diagram as presented in **Fig. 4**. The three-region behavior was clearly observed. These measurements allowed to precisely define the critical shear rates separating these three regimes for each CNC concentration (Orts et al., 1998; Shafiei-Sabet et al., 2012 – 2014 – 2017; Derakhshandeh et al., 2013; Xu et al., 2016; Haywood et al., 2017; Lenfant et al., 2017; Gicquel et al., 2019). As shown in **Fig. 4**, the extent of these three regimes was defined with precision for the three highest concentrations from 8 to 10 wt%: the first shear-thinning regime (I) at the lowest shear rates, the viscosity plateau regime (II), at the intermediate shear rates and the second shear-thinning regime (III) at the highest shear rates. The shear rates applied in these rheometric measurements have been reproduced in the canal type shear flow cell during *in situ* SALS experiment in order to relate the viscosity features described in **Fig. 4** to the structural organization. Equation 1 was used to calculate the corresponding flow rate, Q, applied by the syringe pump, in order to perform each shear flow experiment with the same shear rate $\dot{\gamma}_y$ as the one used during conventional rheometric measurements.

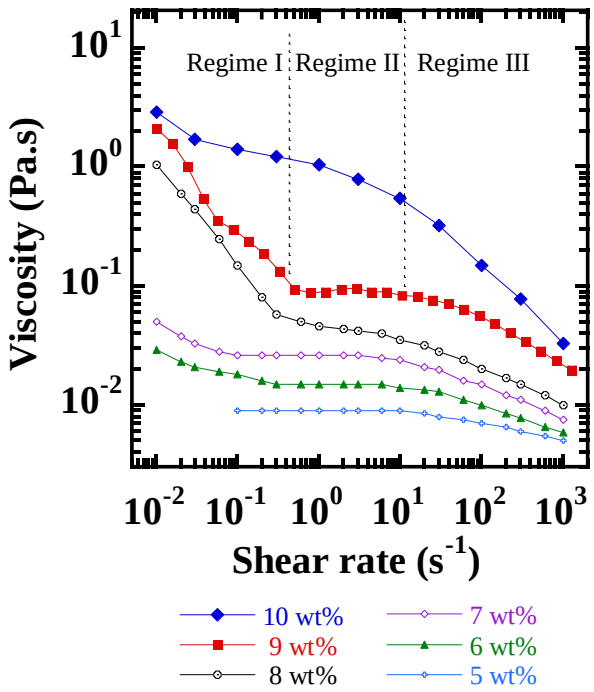

Figure 4. Steady-state flow curve (viscosity as a function of shear rate) of CNC suspensions at different concentrations at 10^{-2} mol L^{-1} NaCl and the evidence for the three-regime behavior. Rheometric measurements were performed in cone-plate geometry at T = 24.5 °C.

3.3.2. Structural Organization at Micrometric Lengthscale: *in situ* SALS under Shear

Starting from a 9 wt% suspension after the rest step of P1, at t = 0 s, SALS patterns consisted of an isotropic ring-like pattern corresponding to a random orientation of the cholesteric assemblies. For the three regimes, one shear rate pertaining to each regime was explored in details. The corresponding SALS time evolution and their analysis by radial, vertical/horizontal sector averaged or annular averaged integrations are presented in **Fig. 5 a-c.**

a) Regime I: shear rate = 0.29 s^{-1}

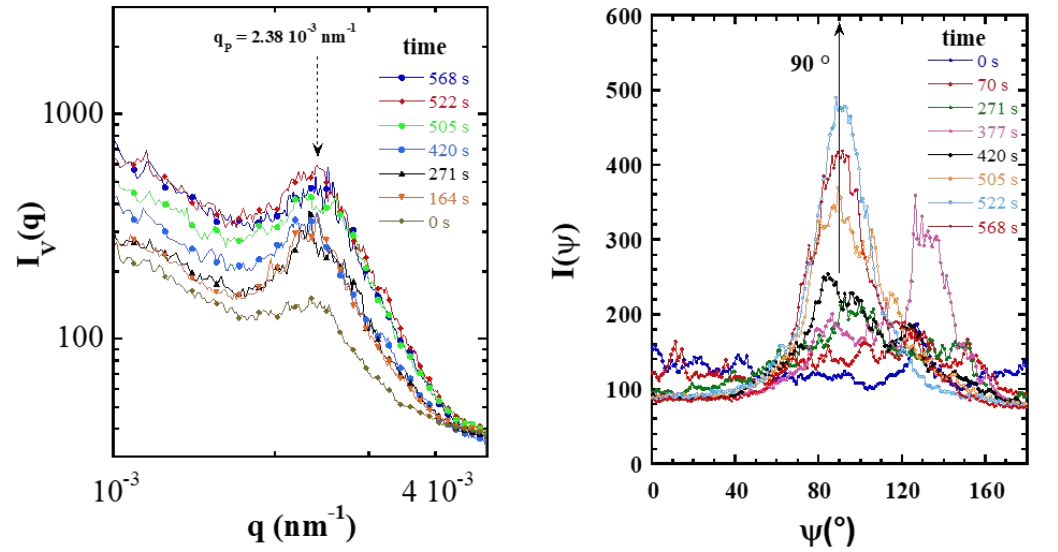

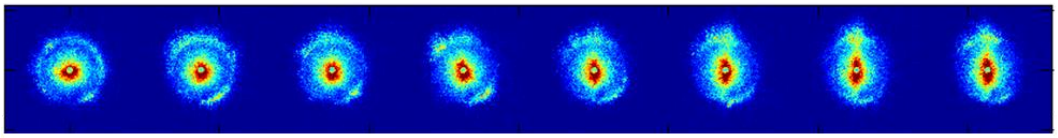

0 s 164 s 271 s 377 s 420 s 505 s 522 s 568 s

322

b) Regime II: shear rate = 13.3 s^{-1}

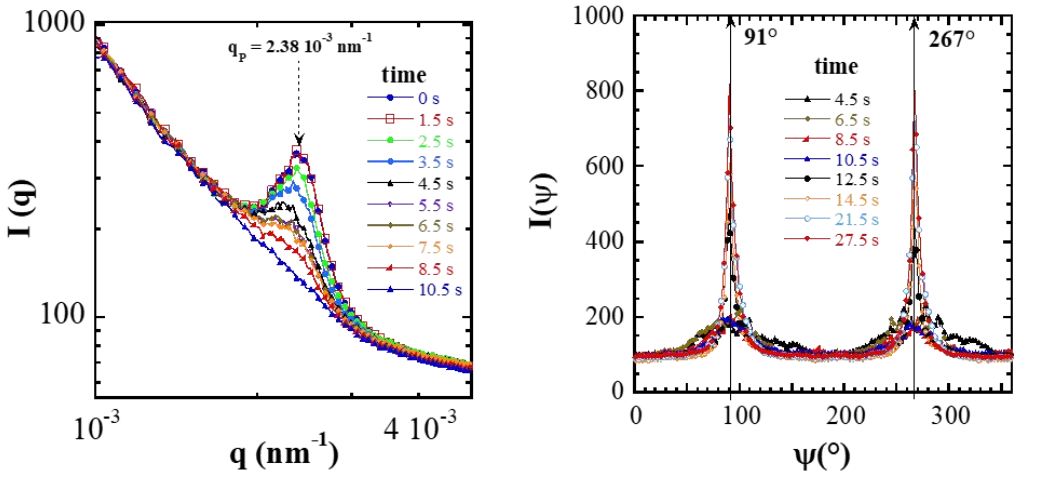

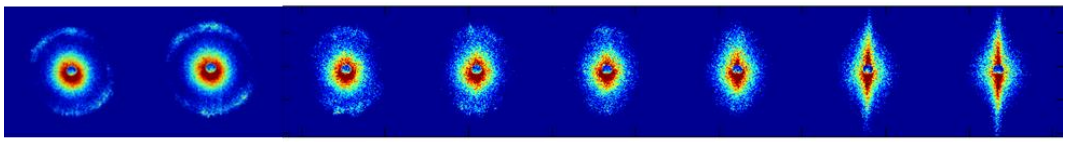

0 s 2.5 s 4.5 s 6.5 s 8.5 s 10.5 s 12.5 s 14.5 s

323

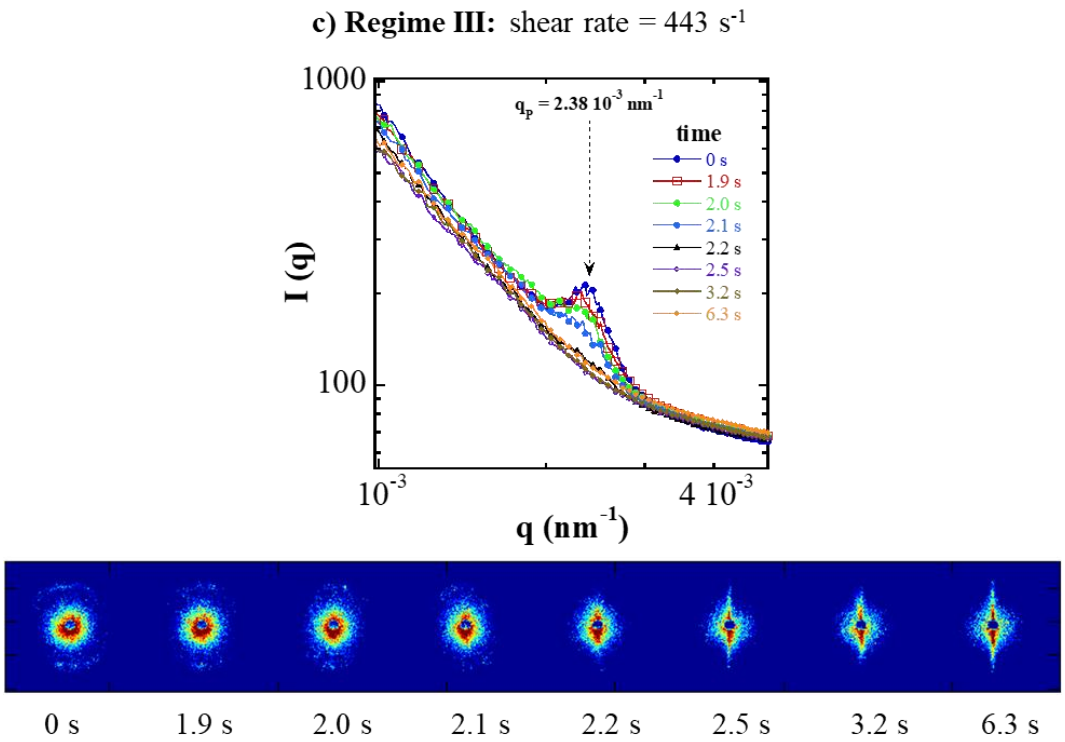

Figure 5. Transient state start flow of the CNC suspensions under *in situ* SALS. Scattering patterns and corresponding azimuthally and radially averaged intensities as a function of time, pertaining to procedure P1 with shear rates corresponding to regimes I (a), II (b), and III (c) for CNC suspensions, C = 9 wt% (ϕ = 5.82 vol%) with 0.01 mol L^{-1} NaCl at T = 25 °C.

Regime I: when a shear flow of rate 0.29 s^{-1} (regime I) was applied, the ring-like pattern observed at rest progressively turned into an anisotropic SALS pattern with a peak intensity oriented along the vertical direction (see **Fig. 5 a**). Both sector and annular averages of the SALS patterns as a function of time confirmed the continuous presence of a correlation peak related to the pitch value and its progressive orientation in the vertical direction, emphasized by the maximum of scattering intensity growing towards ψ = 90 °(**Fig. 5 a**). This evolution was attributed to a gradual orientation with time of the cholesteric phase under flow with the helical axes oriented vertically. A direct *in situ* observation of the mutual orientation of the cholesteric domains with their helical

axes oriented in the vertical direction (perpendicular to the velocity direction) and the conservation of the pitch distance assessing the non-breakup of the cholesteric phase in this regime, are revealed for the first time. This specific mutual orientation of the cholesteric domains releases some internal stress inside the suspension that explains the decrease in viscosity in this first shear thinning regime I. Another remarkable feature of these SALS patterns is that towards the lowest vectors (q = 10^{-3} nm^{-1}) the scattering intensity became anisotropic under shear with a degree of anisotropy increasing with time as depicted by the increase in the I_v curve as a function of time, until a stable orientation was reached (see **Fig. 5a**).

Regime II: For a shear rate of 13.3 s^{-1} shown in **Fig. 5b and Fig. S4**, as for the beginning of regime I, the ring-like pattern of the rest step was progressively replaced by an oriented SALS pattern with a peak intensity that became oriented along the vertical direction over time (t = 4 s). The position of the ring corresponds to a pitch value of 5280 nm (q_P = 2.38 10^{-3} nm^{-1}). Then, the scattering peak corresponding to the initial pitch value progressively weakened and disappeared after t = 10.5 s. At the center of the SALS pattern, the intensity distribution progressively evolved from an isotropic to anisotropic pattern, that became stable when the steady state was reached. Like at the beginning of regime I, this evolution of the SALS patterns was attributed to a progressive orientation of the cholesteric phase under flow, with the helical axis oriented vertically. However, at the higher shear rates of regime II, the disappearance of the pitch signature was well evidenced, which could be interpreted as a progressive disruption of the tactoids in smaller units, whose final size – smaller than the pitch distance – was no longer detectable. This important result clarifies that has been proposed in the literature, which mainly attributed the viscosity plateau regime to the orientation of cholesteric domains along the shear direction and their eventual breakdown (Shafiei-Sabet al., 2012; Derakhshandeh et al., 2013; Shafiei-Sabet et al., 2014; Haywood et al., 2017). In

this study, the *in situ* SALS data collected under shear have clearly shown that the orientation of the cholesteric domains occurred in regime I, while in regime II, the progressive disruption of the tactoids towards a critical micrometer size lower than the pitch distance would be a possible explanation. The interpretation of the orientation of all the cholesteric domains, originally more attributed to regime II by previous works (Shafiei-Sabet al., 2012; Derakhshandeh et al., 2013; Shafiei-Sabet et al., 2014; Haywood et al., 2017) was shifted to regime I based on the current interpretation of SALS measurements.

Regime III: At a shear rate of 443 s^{-1}, the ring-like pattern of the rest step was rapidly replaced by an oriented SALS pattern followed by a progressive decrease of the scattering intensity until the disappearance of the peak as shown in **Fig. 5 c**. These observations are in accordance with a complete breakdown of the cholesteric micrometer sizes tactoids, and emphasize that at this micrometer lengthscale, there is no more structural orientation or organization like the one observed in regime II. This is in complete agreement with previous literature that proposed the merger of liquid crystalline and isotropic domains into a single domain aligned along the flow direction, yielding a uniform texture when observed using polarized light optical microscopy (Shafiei-Sabet al., 2012, 2014; Haywood et al., 2017).

3.3.3. Structural Organization at Nanometer Lengthscale: *in situ* Rheo–SAXS

Rheo-SAXS measurements were performed on samples within a concentration range covering the first two domains of the phase diagram. Two samples of concentrations C = 1.35 wt% (0.84 vol%) and C = 6 wt% (3.783 vol%) belonged to the purely isotropic phase. Another two samples belonged to concentration domain corresponding to co–existence of isotropic and chiral nematic phases: C = 9 wt% (5.82 vol%) and C = 10 wt% (6.49 vol%) for which complex changes in viscosity as a function of shear rate have been reported in the literature (Orts et al., 1998; Shafiei-

Sabet et al., 2012 – 2014 – 2017; Derakhshandeh et al., 2013; Xu et al., 2016; Haywood et al., 2017; Lenfant et al., 2017; Gicquel et al., 2019).

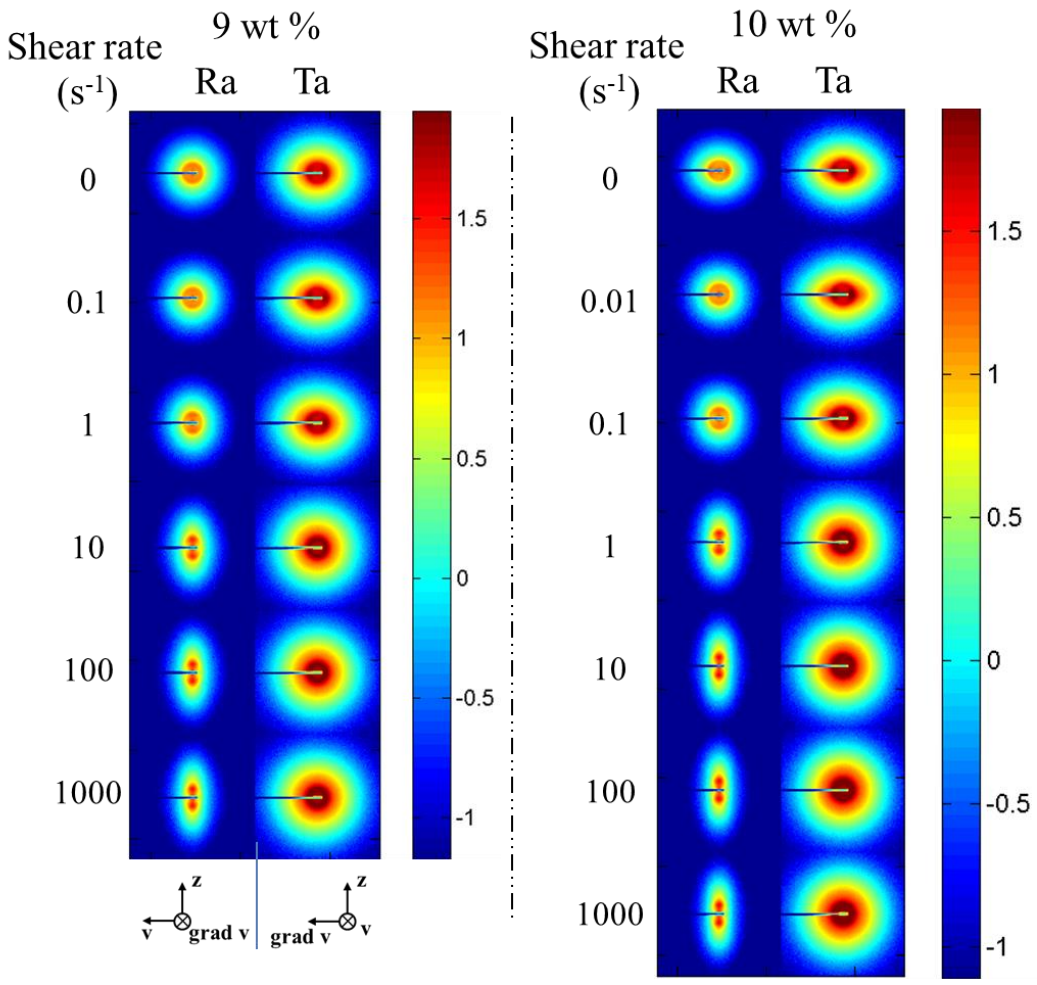

Figure 6. 2D-SAXS patterns from a CNC suspension under steady-state flow for successive steps of applied shear rates, in radial (Ra) and tangential (Ta) positions, corresponding to observation planes (z, v) and (z, *grad* v) (C = 9 wt%, and C = 10 wt%, D = 2 m, 0.01 mol L^{-1} NaCl, T = 24.5 °C).

SAXS measurements were carried out in radial (Ra) and tangential (Ta) configurations to better describe the orientation of the CNCs in the flow field imposed by the two coaxial cylinders of the shear cell as shown in **Fig. 1**. The analysis of the anisotropy was performed by using the MATLAB-

based Small-Angle Scattering Evaluation Tool (SASET) software (Muthig et al., 2013). Specifically, the model-free Principal Component Analysis (PCA) method was chosen, which provides values from 0 (for isotropic suspensions) to 1 (in the case of a completely aligned system).

On a simulated scattering experiment patterns from a collection of independent differently-oriented oblate ellipsoids of revolution, the anisotropy PCA parameter showed a good agreement with the more commonly used P2 second order parameter (Muthig et al., 2013). The advantage of anisotropy PCA is that it can be defined on a wide q-region, is not dependent of a structure-factor (as the one always found in the CNC SAXS patterns associated to the well-defined mean interparticle distance d between CNCs), and its computation does not require additional inputs such as simulated totally aligned scattering patterns (Muthig et al., 2013). The anisotropy and direction of maximum scattering (ψ_0) were calculated via PCA in the (0.15 – 2.4) nm^{-1} q-range and (0.04 - 0.48) nm^{-1} q-range at sample-to-detector distances D = 2 m and 10 m, respectively. One should note that this maximum scattering intensity (ψ_0) can only be defined in the case of anisotropic SAXS patterns and is not defined in the case of isotropic patterns.

The 2D-SAXS patterns of CNC suspensions under shear in steady state conditions are presented in **Fig. 6 and Figs S6, S7** in radial and tangential modes of observation. The corresponding calculated anisotropy parameter and direction of maximum scattering (ψ_0) were plotted in **Fig. 7a** and **7b,** respectively. For comparison the corresponding viscosities as a function of the shear rate are also plotted in **Fig. 7a**.

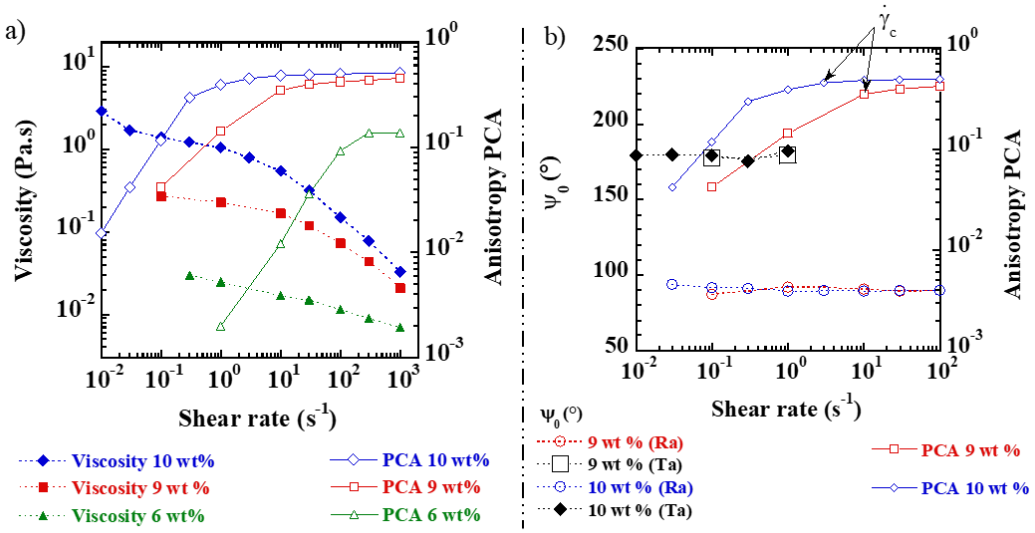

415

416 **Figure 7.** Steady-state flow curves (viscosity as a function of shear rate) of CNC suspensions
417 and corresponding PCA anisotropy parameter (a) and direction of maximum scattering ψ_0
418 (b) calculated from SAXS patterns recorded at different shear rates. The critical shear rate, $\dot{\gamma}_c$
419 defines the limit between regimes II and III. (0.01 mol L^{-1} NaCl, T = 24.5 °C).

420 For the lowest concentration of 6 wt%, corresponding to the complete isotropic phase,
421 Anisotropy PCA regularly increased reaching a plateau at the highest applied shear rates. In the
422 second shear-thinning domain, the increase in anisotropy was mainly attributed to the progressive
423 orientation of all isolated CNCs. For the two highest concentrations at 9 and 10 wt%, both in the
424 co-existing isotropic and cholesteric phase domains, anisotropy PCA increased more sharply in the
425 viscosity plateau region (regime II) until reaching a stable value in the second shear thinning range
426 (regime III) **Fig. 7a**. This type of behavior has previously been observed with CNCs from different
427 origins by rheo-SANS, where a steep increase in the calculated order parameter followed by a
428 plateau above a certain shear rate has been observed (Orts et al., 1998; Haywood et al., 2017). This
429 evolution of the order, or anisotropy parameter, agrees with the theory proposed by Onogi and
430 Asada (1980) in which domains start to break up in the intermediate viscosity plateau domain
431 (regime II), whereas individual rods are free to align in the second shear thinning region (regime

III). Present data coherently follow the same trends: the sharp increase would be attributed to the breakdown of the tactoids as evidenced by SALS at larger lengthscales and the subsequent reorientation of the CNCs reinforced by the orientation of the isolated CNCs in the isotropic phase.

The evidence of the disruption of the micrometric tactoids in regime II observed by SALS, is reinforced by the quantitative analysis of the rheo-SAXS measurements performed in radial and tangential modes of observation. In radial mode of observation for the two highest concentrations at 9 and 10 wt%, an increase of scattering intensity is observed in the vertical direction (*z*) with increasing shear rate (**Fig. 6 and Figs S6, S7)**, corresponding to direction of maximum scattering ψ_0 of about 90° (**Fig. 7b)**. This increase of scattering intensity can be attributed to a partial alignment of the CNCs with their director along the y direction or velocity *v*. It is due to the reinforcement of fluctuations in particle concentrations along *z* generated by the alignment of the CNCs along *v*. On the contrary, in tangential mode of observation, an increasing anisotropy of the SAXS patterns along the grad *v* direction is clearly seen until the critical shear rate, $\dot{\gamma}_c$ (**Figs. 6** and **7b)**. Indeed, a $\dot{\gamma}_c$ of about 10 s^{-1} at 9 wt % or 3 s^{-1} at 10 wt% belonging to the end of regime II or beginning of regime III in **Figs. 6** and **7b**, demarcates two specific features of the SAXS patterns. Above $\dot{\gamma}_c$, the SAXS pattern is isotropic. Below $\dot{\gamma}_c$, the SAXS patterns in tangential mode of observation are elongated along *grad v* corresponding to direction of maximum scattering ψ_0 of about 180° (**Fig. 7b)**. This feature is well in accordance with some elongated micrometer tactoids flowing and oriented along the velocity *v* as suggested by the SALS analysis and as already observed by rheo-SAXS on flowing clay sepiolite fibers in the same tangential mode of observation (Pignon et al., 2009). The increase of intensity along the grad *v* direction is due to the reinforcement of fluctuations in the elongated micrometer tactoids oriented along *v*. This orientation of elongated

tactoids under shear has also been proposed by Park et al. (2014). Above $\dot{\gamma}_c$, the SAXS patterns in tangential mode of observation became isotropic with an annular form. This is consistent with a progressive breakdown of the micrometer tactoids elongated in smaller units which disintegrate and melt to isolated CNCs at the highest shear rate. This observation is also in agreement with a huge decrease of the scattering intensity in SALS until the disappearance of significant scattering from the sample at the highest shear rates in regime III. These observations are also supported by recent works (Rosén et al., 2020) which studied in detail the projected flow-induced orientation distributions of dispersed CNCs in a square channel flow using scanning microbeam SAXS. From the good agreement between simulations giving the orientation distribution function, and SAXS measurements, they show that at low flow rates, CNCs are highly aligned, indicating that particle-particle interactions inhibit the effects of Brownian rotational diffusion and collectively respond to the shear. They concluded that for semidilute concentration domains, CNCs move collectively into large ellipsoidal tactoids, which themselves have a lower aspect ratio than individual particles and thus spend less time aligned along the flow direction.

At highest velocity gradients, when leaving the viscosity plateau to reach the second shear thinning region, above $\dot{\gamma}_c$ the anisotropy PCA stabilizes after reaching a maximum level towards an equilibrium value. This stabilization of the orientation level is consistent with the fact that in this region all nanocrystals (irrespective of the phase they initially belonged to) flow in parallel, like in a nematic arrangement and allow the system to flow more easily while maintaining an identical orientation of each crystal. The evolution of the anisotropy PCA as a function of shear rate and concentration emphasized that an optimal alignment was reached when CNCs in chiral-nematic domains evolve towards a nematic organization.

Another interesting feature is that the position of the maximum of intensity of the azimuthal averaged (**Fig. S5a**) or sector (**Fig. S5b**) averaged scattering intensity occurs at the same $q = q_{max}$ = 0.2 nm^{-1} associated to a well-defined interparticle distance of about $d = 2\pi/q_{max}$ = 31.4 nm (at C = 9 wt%), regardless of the applied shear rate and whether the observation is made in radial or tangential mode. The same features have been observed in the past using CNCs from different botanical sources (Orts et al., 1998). This clearly indicates the typical behavior of a flowing liquid crystal, for which objects remain at a well-defined mean distance. Moreover, above $\dot{\gamma}_c$, the scattering pattern in the tangential configuration remained isotropic. This shows that the CNCs were oriented along horizontal current lines without adopting any particular organization perpendicular to the flow (no higher order peaks or hexagonal packing). This corresponds to a uniaxial orientation of the particles with a strong stabilization of the orientation of these objects. These results on the structural organization of CNCs under shear are different from those observed for disk-shaped beidellite clay systems (Bihannic et al., 2010, Philippe et al., 2011) or sepiolite clay fibers (Pignon et al., 2009). In these latter cases, the anisotropy of SAXS patterns showed different elongations in radial and tangential observations, which was attributed to a biaxial orientation of the particles.

3.2.3 Complete Description of the Global Structural Organization Pertaining to the three-regime-behavior (Combined SALS and SAXS data)

For the three regimes, the steady-state measurements obtained with procedure P2 have allowed confirming the general behavior depicted in start-flow experiments with procedure P1. As shown in **Figs. S3, S4, S8, S9**, the nanometric CNCs were oriented under flow until large micrometer lengthscales corresponding to the q-range (from $L_{y1} = 2\pi/q_{y1}$= 15.7 µm to $L_{y2} = 2\pi/q_{y2}$ = 1.05 µm) explored by SALS. From SALS and SAXS data collected within a shear rates range from 10^{-2} to

10^3 s^{-1} and CNC concentration in the co-existence region of the phase diagram (9wt%), in conjunction with the viscosity/shear rate rheometric measurements, a complete description of this flow curve with the well-known three-regime behavior can be obtained. The global structural organization pertaining to the three-regime-behavior is schematized in **Fig. 8**. The first shear-thinning part in regime I at the lowest shear rates, corresponds to a progressive disruption of the liquid crystalline domains to form micrometer sized tactoids aligned towards the velocity direction with an internal cholesteric organization of the CNCs and the helical axes oriented vertically (evidenced by SALS and the presence of the pitch in vertical direction). Upon reaching the viscosity plateau, in the intermediate shear rate domain (regime II), the SALS pattern shows the breakdown of the tactoids into smaller units down to a critical size smaller than the pitch value. The mean anisotropy parameter calculated from the SALS patterns exhibit a maximum value in this plateau regime II, attributed to a maximum of the alignment of these smaller units of tactoids along the velocity direction in this regime. The SAXS measurements confirm the orientation of the smaller units of tactoids in accordance with the elongated anisotropy of the SAXS patterns along the grad *v* direction in tangential mode of observation, associated to the huge increase of anisotropy PCA. None of these measurements allow to discriminate two possible CNC organizations within the smaller and smaller tactoids. This would be either some CNCs still associated in helical arrangement but with a size lower than the initial pitch of the suspension at rest, or the unwinding of the cholesteric organization towards a nematic-like arrangement as reported in previous works (Gray et al. 2016; Schütz et al. 2020), or even a combination of this two. The third shear-thinning part at the highest shear rates (regime III) corresponds to the complete breakdown of the smaller units of tactoids as evidence by SALS where no significant scattering intensity is detected. The SAXS observations at nanometer lengthscale display a stabilization of the orientation level

consistent with the parallel flowing of all nanocrystals along the velocity direction like into a nematic arrangement.

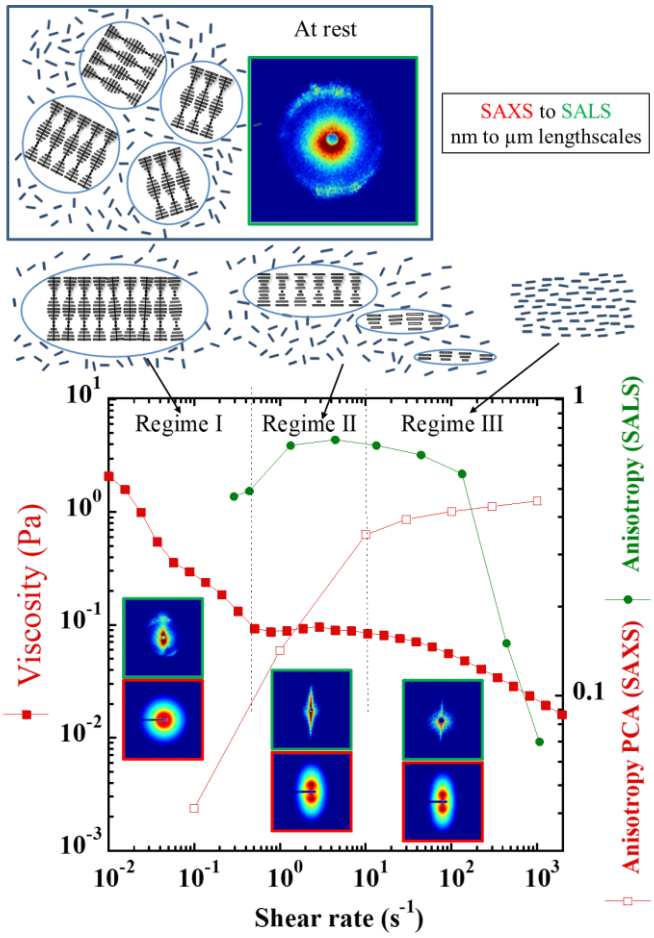

Figure 8. Schematic description of CNC suspensions from rest to increasing applied shear rates, displaying transitions from isotropically distributed "cholesteric tactoids" at rest, to aligned "cholesteric tactoids" in regime I, to fragmentation of micrometer size tactoids in regime II, to isolated oriented CNCs in regime III. Viscosity/shear-rate curve from rheometric measurements, anisotropy parameter deduced from SAXS and SALS measurements. Corresponding *in situ* SAXS and SALS patterns (C = 9 wt%, 5.82 vol%, 0.01 mol L^{-1} NaCl at T = 24.5 °C). Blue circles or blue ellipses drawn in the scheme identify the cholesteric phase domains or tactoids with respect to the isotropic phase.

3.4. Buildup Mechanisms of CNC Suspensions After Cessation of Flow

Two observations were carried out to elucidate the build-up phenomena after a high shear.

First, at nanometer scale by rheo-SAXS: after a high shear at 1000 s^{-1}, the viscosity and SAXS patterns were recorded over time under a very low 10^{-2} s^{-1} shear rate. This allowed having a torque measurement to follow the evolution of viscosity and correlate it with SAXS measurements during relaxation and return to equilibrium of the system under a low shear rate (**Fig. 9**). Two kinetics of relaxation were identified corresponding to two marked changes in viscosity and PCA parameter evolutions. On the viscosity plot, a first relaxation regime of the order of 700 s (around 12 min) was followed by a second longer relaxation regime, established on time scales of 30 min. The anisotropy as quantified by PCA perfectly followed these two processes with a first marked decrease in anisotropy over the first 700 s, followed by a second, slower kinetics with a decrease in anisotropy over time on longer timescales of about 30 min.

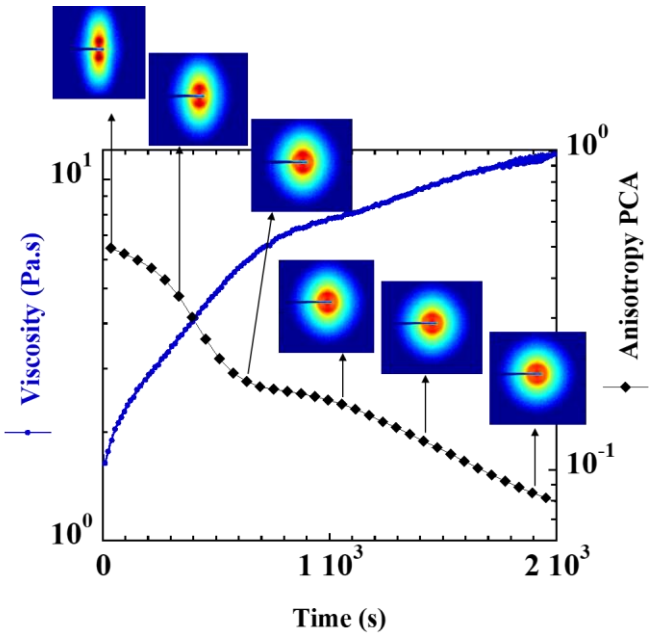

Figure 9. Relaxation process of a CNC suspension under shear of 10^{-2} s^{-1} after pre-shear at 1000 s^{-1}. Time dependent evolution of viscosity and corresponding anisotropy PCA parameter, from the simultaneously recorded SAXS patterns (C = 10 wt%, 6.49 vol% with sample-to-detector distance D = 2 m and T = 24.5 °C).

Second, at large lengthscales by SALS according to procedure P3: after a high shear rate of 1068 s^{-1} the shear was stopped and the SALS patterns were registered as a function of time (**Figs. 10** and **S10, S11**).

From SALS measurements, when a shear rate of 1068 s^{-1} was applied, no significant scattering signal induced by structural organization was detected. This suggests that CNCs were flowing independently, with an orientation that was established only at the CNC nanometer scale as shown by SAXS data. After cessation of shear flow the relaxation process followed three steps with different dynamics.

Step 1: when the shear was stopped, surprisingly, it took only a few seconds for the micrometer-scale organization to recover, thanks to a fast relaxation process. An anisotropic SALS pattern with an oval shape oriented along the vertical direction was observed at t = 19 s, which evolved over a few minutes as depicted in **Fig. 10a**. The corresponding SAXS patterns over this first relaxation step, are also elongated vertically, *i.e.* perpendicular to the velocity. These multiscale observations are in accordance with the fast build-up of a largescale oriented nematic domain extending from nanometer to micrometer scales. This surprising effect can be attributed to liquid-crystal characteristic behavior, of these colloidal particles, for which the constant interparticle distance as well as the homogeneous interparticle interactions between the crystals promote a rapid re-organization of the particles.

572 **Step 2:** during the following seconds up to first 15 min, the central region of the SALS patterns
573 became progressively isotropic and simultaneously manifested the gradual appearance of a
574 scattered intensity peak along the vertical direction that grew in size and intensity (**Fig. 10**). At
575 time 675 s the appearance of the q_P is evidenced. This q_P value corresponds well to that of the
576 dispersion at rest, which is related to the pitch of the cholesteric domains in the sample. It is
577 consistent with the reorganization of cholesteric tactoids (Wang et al., 2016; Wang and
578 MacLachlan 2018; Tran et al., 2018; Liu et al., 2019) with a specific vertical orientation of their
579 helical axis. These observations are supported by recent polarized light microscopy observations
580 (Gray and Mu 2016) who addressed the question of how the texture of samples placed between a
581 microscope slide and cover glass changes with relaxation time when evaporation is inhibited. They
582 observed a transitory nematic-like texture that was induced by shear during the preparation of the
583 sample for polarized light microscopy. From their optical observation, they suggested that there is
584 an alternative mechanism for shear relaxation of CNC suspensions involving an intermediate stage
585 between nematic and chiral nematic ordered suspensions: a twist-bend-like intermediate and not
586 an untwisting of the chiral nematic phase (Gray and Mu 2016).

587 In parallel to the scattering intensity evolution around this q_P, the center of the SALS patterns
588 that was anisotropic and oriented in the vertical direction after a few seconds, slowly became
589 isotropic as shown by the annular integration in **Fig. 10b**. This evolution at micrometer lengthscale
590 is in good agreement with the rheo-SAXS measurements, emphasizing a fast kinetic of relaxation
591 up to 700 s for which the anisotropy PCA parameter sharply decreased while a fast increase in
592 viscosity was measured (**Fig. 9**).

593 This mechanism of relaxation could be associated to a demixing process that corresponds to the
594 isotropic and cholesteric phase separation with an induction time (about 675 s). Letting et al. (2005)

595 have studied in detail the different demixing process of the nematic-isotropic phase transition of
596 rodlike colloids after a quench from the flow-induced fully nematic state. They highlighted that the
597 two mechanisms of phase separation (spinodal decomposition and nucleation-and-growth) can be
598 distinguished during the initial stages of phase separation from (i) the difference in morphology
599 (interconnected structures versus growth of isolated nuclei) and (ii) the delay time before the phase
600 separation sets in (no delay time for spinodal decomposition and a finite induction time for
601 nucleation-and-growth). The relaxation features evidenced in this work on CNC suspensions
602 clearly exhibit an induction time associated to the appearance of a pitch revealing the formation of
603 cholesteric tactoids, which allowed demonstrating that the most probable mechanism of relaxation
604 is associated to a nucleation-and-growth process.

605 **Step 3:** Following this continuous relaxation process, a third longer relaxation took place over
606 time up to 1668 s. The annular averages of these patterns during relaxation show a progressive
607 evolution of the angular distribution of the scattered intensity around this peak, over a long
608 timescale as presented in **Fig. 10b**. After about 30 min, an isotropic distribution is reached, giving
609 rise to a ring-like scattering pattern equivalent to that of a suspension at rest. In the same manner
610 at nanometer lengthscale a slower evolution of the increase of viscosity and decrease of anisotropy
611 parameters is evidenced until 30 min of relaxation (**Fig. 9**).

612

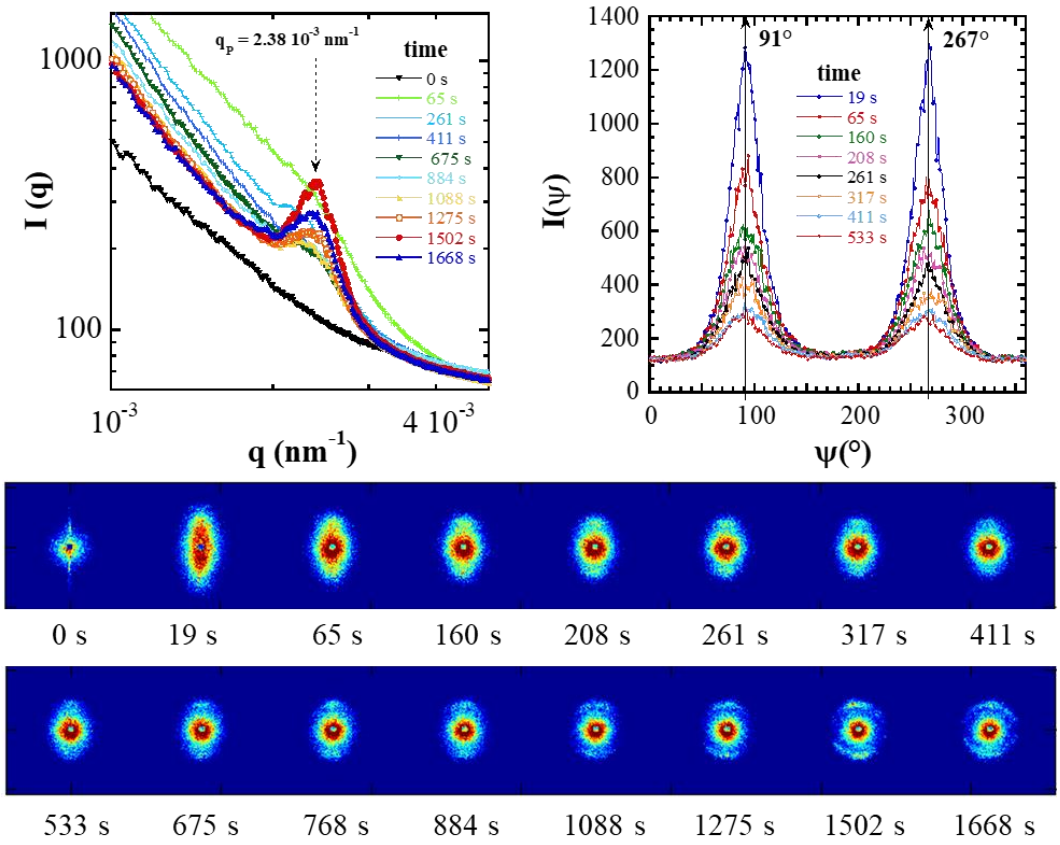

Figure 10. Transient state relaxation of the CNC suspensions under *in situ* SALS. Scattering patterns and corresponding azimuthal (a) and annular (b) average intensities as a function of time, pertaining to procedure P3 with initial shear rates belonging to regime III at 1068 s^{-1}. C = 9 wt% (ϕ = 5.82 vol%) with 0.01 mol L^{-1} NaCl at T = 25 °C.

4. Conclusions

In this work, the complex three-regime rheological behavior of CNC suspensions under shear flow, typical of liquid crystalline systems, has been studied with a multi-lengthscale approach, in the coexistence regime of isotropic and cholesteric phases, from the size of elementary CNCs (by rheo-SAXS) to that of their assemblies into a cholesteric organization (by SALS under flow). The change in viscosity identified in rheometric measurements has been correlated with structural

parameters over a wide lengthcales (including anisotropy parameters, CNC interparticle and presence or absence of the cholesteric pitch) as a function of time and shear rate, in steady and transient flows (start flow) as well as during the system relaxation after cessation of shear.

Thanks to SALS data under shear flow, the changes in chiral nematic organization, and the disappearance and reappearance of pitch under flow and during relaxation, respectively have been described for the first time. The combination with the Rheo-SAXS results in radial and tangential modes of observation clarified the shear-induced structural evolutions and dynamic changes in chiral nematic organization along the well-known three-regions behavior.

Several breakthrough have been achieved thanks to this multiscale characterization. First, it has been shown that at lowest shear rates of shear thinning regime I, during the first gradual disruption of large liquid crystalline domains into smaller micrometer-sized tactoids, the cholesteric domains orient with their helical axis aligned perpendicular to the flow direction. This orientation effect had previously been attributed to the plateau regime II (Orts et al., 1998; Shafiei-Sabet al., 2012; Derakhshandeh et al., 2013; Shafiei-Sabet et al., 2014; Haywood et al., 2017). Consequently, this result clarifies what has been previously proposed in the literature, by shifting the current interpretation of the organization of CNCs to lower shear rate ranges.

Second, the presence of sub-micrometer sized elongated tactoids flowing and oriented along the velocity have been clearly evidenced in the viscosity plateau regime II, thanks to the joint interpretation of 2D-SAXS and 2D-SALS patterns. The disappearance of the pitch distance in this domain was revealed for the first time, which demonstrates that the size of the micrometer-size elongated tactoids are smaller than the pitch.

Third, the buildup mechanisms, upon cessation of the high shear corresponding to regime III have been highlighted for the first time in the pertinent micrometer lengthscale. The appearance of anisotropic SAXS and SALS patterns elongated vertically, i.e. perpendicular to the previous flow

direction, evidenced an impressive fast reassembling of CNCs into a nematic-like organization with a parallel orientation of CNCs along the previous velocity direction which was characterized on a broad range of lengthscales (from nanometer to micrometer). After that, surprisingly, a slower mechanism, associated to a slower increase in viscosity, was established: this largescale oriented nematic organization evolved into orientated cholesteric micrometric domains with their helical axes aligned perpendicular to the previous flow direction. This relaxation step is associated to a demixing process which corresponds to the isotropic and cholesteric phase separation with an induction time of about 15 min. This suggested that the mechanism of relaxation was probably mainly associated to a nucleation-and-growth process. Finally, a much slower reorganization of these large oriented domains took place towards an isotropic distribution of cholesteric arrangements to build up the final isotropic equilibrium structure of CNC suspensions at rest.

The approach used in this work have shed new light on both particle organization at the relevant lengthscale and structuration mechanisms in CNC suspensions under shear flow. This approach could be applied to better understand buildup mechanisms during nanocomposite elaboration involving shear flow processing, in order to fabricate nanocellulose-based materials with optimal control of the structural and functional properties as conductive, barrier, mechanical or optical properties.

Acknowledgement

We sincerely thank Erwan Paineau (LPS, Saclay) for constructive discussions and William Chèvremont (Laboratoire Rhéologie et Procédés) for his great help in improvement of the SALS set-up. We also thank Jacques Gorini (ESRF, Grenoble), Didier Blésès, Frédéric Hugenell and Eric Faivre (Laboratoire Rhéologie et Procédés) for technical assistance. ESRF is acknowledged for

provision of synchrotron beamtime (proposal SC-4177 and in-house beam time), as well as the ICMG-NanoBio platform (FR 2607, Grenoble) for granting access to the electron microscopy facility. This work has received the financial support of Institut Carnot PolyNat (Investissements d'Avenir - grant agreement #ANR-16-CARN-0025-01) and was carried out within the framework of the RheoNat and NanoCompUV projects. LRP is part of LabEx Tec21 (Investissements d'Avenir - grant agreement no. ANR-11-LABX-0030) and CERMAV is part of LabEx Arcane and CBH-EUR-GS (Investissements d'Avenir - grant agreement #ANR-17-EURE-0003). Both laboratories are part of the Glyco@Alps programme (Investissements d'Avenir - grant agreement #ANR-15-IDEX-02).

References

Alizadehgiashi, M., Khabibullin, A., Li, Y., Prince, E., Abolhasani, M., Kumacheva, (2018). E. Shear-Induced Alignment of Anisotropic Nanoparticles in a Single-Droplet Oscillatory Microfluidic Platform. *Langmuir*, *34*, 322-330.

Bercea, M., Navard, P. (2000). Shear dynamics of aqueous suspensions of cellulose whiskers. *Macromolecules* , *33*, 6011–6016.

Bihannic, I., Baravian, C., Duval, J.F.L., Paineau, E., Meneau, F., Levitz, P., de Silva, J.P., Davidson, P., Michot, L.J. (2010). Orientational order of colloidal disk-shaped particles under shear-flow conditions: a rheological-small-angle X-ray scattering study. *J. Phys. Chem. B*, *114*, 16347–16355.

Derakhshandeh, B., Petekidis, G., Shafiei-Sabet, S., Hamad, W.Y., Hatzikiriakos, S.G. (2013). Ageing, yielding, and rheology of nanocrystalline cellulose suspensions. *J. Rheol.*, *57*, 131–148.

695 Domingues, R.M.A., Gomes, M.E., Rei, R.L. (2014). The potential of cellulose nanocrystals in
696 tissue engineering strategies. *Biomacromolecules*, *15*, 2327–2346.
697 Dong, X.M., Kimura, T., Revol, J.-F., Gray, D.G. (1996). Effects of ionic strength on the
698 isotropic−chiral nematic phase transition of suspensions of cellulose crystallites. *Langmuir*,
699 *12*, 2076–2082.
700 Dufresne, A. (2017). Nanocellulose: From Nature to High Performance Tailored Materials, 2nd
701 ed., Walter de Gruyter GmbH: Berlin/Boston.
702 Ebeling, T., Paillet, M., Borsali, R., Diat, O., Dufresne, A., Cavaillé, J.-Y., Chanzy, H. (1999).
703 Shear-induced orientation phenomena in suspensions of cellulose microcrystals, revealed by
704 small angle X-ray scattering. *Langmuir*, *15*, 6123–6126.
705 Eichhorn S. J. Young R.J., and Davies G. D. (2005). Modeling crystal and molecular deformation
706 in regenerated cellulose fibers. *Biomacromolecules*, *6*, 507–513.
707 Frka-Petesic, B., Radavidson, H., Jean, B., Heux, L. (2017). Dynamically controlled iridescence of
708 cholesteric cellulose nanocrystal suspensions using electric fields. *Adv. Mater.*, *29*, 1606208.
709 Gicquel, E., Bras, J., Rey, C., Putaux, J.-L., Pignon, F., Jean, B., Martin, C. (2019). Impact of
710 sonication on the rheological and colloidal properties of highly concentrated cellulose
711 nanocrystal suspensions. *Cellulose*, *26*, 7619–7634.
712 Gray, D.G., Mu, X. (2016). Twist–bend stage in the relaxation of sheared chiral nematic
713 suspensions of cellulose nanocrystals. *ACS Omega*, *1*, 212–219.
714 Haywood, A.D., Weigandt, K.M., Saha, P., Noor, M., Green, M.J., Davis V.A. (2017). New
715 insights into the flow and microstructural relaxation behavior of biphasic cellulose nanocrystal
716 dispersions from RheoSANS. *Soft Matter*, *13*, 8451–8462.

Jin, Y., Hengl, N., Baup, S., Pignon, F., Gondrexon, N., Sztucki, M., Romdhane, A., Guillet, A., Aurousseau, (2015). M. Ultrasonic assisted cross-flow ultrafiltration of starch and cellulose nanocrystals suspensions: Characterization at multi-scales. *Carbohydr. Polym.*, *124*, 66–76.

Kargarzadeh, H., Huang, J., Lin, N., Ahmad, I., Mariano, M., Dufresne, A., Thomas, S., Gałęski, A. (2018). Recent developments in nanocellulose-based biodegradable polymers, thermoplastic polymers, and porous nanocomposites. *Prog. Polym. Sci.*, *87*, 197−227.

Lagerwall, J.P.F., Schütz, C., Salajkova, M., Noh, J., Park, J.H., Scalia, G., Bergstrom, L. (2014). Cellulose nanocrystal-based materials: from liquid crystal self-assembly and glass formation to multifunctional thin films. *Npg Asia Materials*, *6*, e80.

Lenfant, G., Heuzey, M.-C., van de Ven, T.G.M., Carreau, P.J. (2017). A comparative study of ECNC and CNC suspensions: effect of salt on rheological properties, *Rheol. Acta*, *56*, 51–62.

Lettinga, M.P., Kang, K., Imhof, A., Derks, D., Dhont, J. K G. (2015). Kinetic pathways of the nematic–isotropic phase transition as studied by confocal microscopy on rod-like viruses; *J. Phys.: Condens. Matter, 17*, S3609–S3618.

Liu, Y., Schütz, C., Salazar-Alvarez, G., Bergström, L. (2019). Assembly, gelation, and helicoidal consolidation of nanocellulose dispersions. *Langmuir*, *35*, 3600–3606.

Mitov, M. (2017). Chlolesteric liquid crystals in living matter. *Soft Matter*, *13*, 4176–4209.

Muthig, M., Prévost, S., Orglmeister, R., Gradzielski, M. (2013). SASET: A program for series analysis of small-angle scattering data. *J. Appl. Crystal*, *46*, 1187–1195.

Narayanan, T., Sztucki, M., Van Vaerenbergh, P., Léonardon, J., Gorini, J., Claustre, L., Sever, F.,Morse, J., Boesecke, P. (2018). A multipurpose instrument for time-resolved ultra-small-angle and coherent X-ray scattering. *J. Appl. Crystal., 51*, 1–14.

Onogi, S., Asada, T. (1980). Rheology and rheo-optics of polymer liquid crystals. In: Astarita G., Marrucci G., Nicolais L. (eds) Rheology. Springer, Boston, MA.127–147.

741 Orts, W.J., Godbout, L., Marchessault, R.H., Revol, J.-F. (1998). Enhanced ordering of liquid
742 crystalline suspensions of cellulose microfibrils: A small angle neutron scattering study.
743 *Macromolecules*, *31*, 5717–5725.
744 Panine, P., Gradzielski, M., Narayanan, T. (2003). Combined rheometry and small-angle X-ray
745 scattering. *Rev. Sci. Instrum.*, *74*, 2451–2455.
746 Park, J.H., Noh, J., Schütz, C., Salazar-Alvarez, G., Scalia, G., Bergström, L. and Lagerwall, J.P.F.
747 (2014). Macroscopic Control of Helix Orientation in Films Dried from Cholesteric Liquid-
748 Crystalline Cellulose Nanocrystal Suspensions. *ChemPhysChem*, *15*, 1477-1484.
749 Philippe, A.M., Baravian, C., Imperor-Clerc, M., De Silva, J., Paineau, E., Bihannic, I., Davidson,
750 P.; Meneau, F., Levitz, P., Michot, L.J. (2011). Rheo-SAXS investigation of shear-thinning
751 behaviour of very anisometric repulsive disc-like clay suspensions. *J. Phys.-Condens. Matter*,
752 *23*, 194112.
753 Piau, J.M., Dorget, M., Palierne, J.F. (1999). Shear elasticity and yield stress of silica–silicone
754 physical gels: Fractal approach. *J. Rheol.*, *43*, 305–314.
755 Pignon, F., Magnin, A., Piau, J.M., Belina, G., Panine, P. (2009). Structure and orientation
756 dynamics of sepiolite fibers - poly(ethylene oxide) aqueous suspensions under extensional and
757 shear flow, probed by in situ SAXS. *Rheol. Acta*, *48*, 563–578.
758 Qi, W., Yu, J., Zhang, Z., Xu, H-N. (2019). Effect of pH on the aggregation behavior of cellulose
759 nanocrystals in aqueous medium. *Mater. Res. Express*, *6*, 125078.
760 Revol, J.-F., Bradford, H., Giasson, J., Marchessault, R.H., Gray D.G. (1992). Helicoidal self-
761 ordering of cellulose microfibrils in aqueous suspension. *Int. J. Biol. Macromol.*, *14*, 170–172.
762 Rey, C., Hengl, N., Baup, S., Karrouch, M., Gicquel, E., Dufresne, A., Djeridi, H., Dattani, R., Jin,
763 Y., Pignon, F. (2019). Structure, rheological behavior and in situ local flow-fields of cellulose

nanocrystal dispersions during cross-flow ultrafiltration. *ACS Sustain. Chem. Eng.*, *7*, 10679−10689.

Rosén, T, Wang, R., Zhan C., He, H., Chodankar, S., Benjamin, S., Hsiao, B.S. (2020). Cellulose nanofibrils and nanocrystals in confined flow: Single-particle dynamics to collective alignment revealed through scanning small-angle x-ray scattering and numerical simulations. *Phys. Rev. E*, *101*, 032610.

Sanchez-Botero, L., Dimov, A.V., Li, R., Smilgies, D.-M., Hinestroza, J.O. (2018). In situ and real-time studies, via synchrotron X-ray scattering, of the orientational order of cellulose nanocrystals during solution shearing. *Langmuir*, *34*, 5263−5272

Schütz, C., Agthe, M., Fall, A. B., Gordeyeva, K., Guccini, V., Salajková, M., Plivelic, T. S., Lagerwall, J. P. F., Salazar-Alvarez, G., Bergström, L. (2015). Rod packing in chiral nematic cellulose nanocrystal dispersions studied by small-angle X-ray scattering and laser diffraction. *Langmuir, 31*, 6507–6513.

Semeraro, E.F., Hengl, N., Karrouch, M,, Michot, L.J., Paineau, E., Jean, B., Putaux, J.-L., Lancelon-Pin, C., Sharpnack, L., Pignon, F. (2020). Layered organization of anisometric cellulose nanocrystals and beidellite clay particles accumulated near the membrane surface during cross-flow ultrafiltration: In situ SAXS and ex situ SEM/WAXD characterization. *Colloid Surface A*, *584*, 124030.

Shafiei-Sabet, S., Hamad, W.Y., Hatzikiriakos, S.G. (2014). Ionic strength effects on the microstructure and shear rheology of cellulose nanocrystal suspensions. *Cellulose*, *21*, 3347–3359.

Shafiei-Sabet, S., Hamad, W.Y., Hatzikiriakos, S.G. (2012). Rheology of nanocrystalline cellulose aqueous suspensions. *Langmuir, 28*, 17124–17133.

787 Siqueira, G., Bras, J., Dufresne, A. (2010). Cellulosic bionanocomposites: A review of preparation,
788 properties and applications. *Polymers*, *2*, 728–765.
789 Son, Y. (2007). Determination of shear viscosity and shear rate from pressure drop, and flow rate
790 relationship in a rectangular channel. *Polymer*, *48,* 632–637.
791 Sztucki M., Narayanan T. (2007). Development of an ultra-small-angle X-ray scattering instrument
792 for probing the microstructure and the dynamics of soft matter, *J. Appl. Cryst.*, *40*, 459–462.
793 Tang A., Li, J., Li, J., Zhao, S., Liu, W., Liu, T., Wang, J., Liu, Y. A. (2019).
794 Nanocellulose/PEGDA aerogel scaffolds with tunable modulus prepared by stereolithography
795 for three-dimensional cell culture. *Biomater. Sci. Polym.*, *30*, 797–814.
796 Thomas, B., Raj, M.C., Athira, K.B., Rubiyah, M.H, Joy, J., Moores, A., Drisko, G.L., Sanchez, C.
797 (2018). Nanocellulose, a versatile green platform: from biosources to materials and their
798 applications. *Chem. Rev.*, *118*, 11575–11625.
799 Tran, A., Hamad, W.Y., MacLachlan, M.J. (2018). Tactoid Annealing improves order in self-
800 assembled cellulose nanocrystal films with chiral nematic structures. *Langmuir*, *34* (2), 646–
801 652.
802 Ureña-Benavides, E.E., Ao, G., Davis, V.A., Kitchens, C.L. (2011). Rheology and phase behavior
803 of lyotropic cellulose nanocrystal suspensions. *Macromolecules*, *44*, 8990–8998.
804 Wang, P., Hamad, W., MacLachlan, (2016). M. Structure and transformation of tactoids in
805 cellulose nanocrystal suspensions. *Nat. Commun.*, *7*, 11515.
806 Wang, P.-X., MacLachlan, M.J. (2018). Liquid crystalline tactoids: ordered structure, defective
807 coalescence and evolution in confined geometries. *Phil. Trans. R. Soc. A , 376*, 20170042.
808 Xu, H.-N., Tang, Y.-Y., Ouyang, X.-K. (2017). Shear-induced breakup of cellulose nanocrystal
809 aggregates. *Langmuir, 33*, 235–242.

Xu, Y., Atrens, A., Stokes, J.R. (2020). A review of nanocrystalline cellulose suspensions: Rheology, liquid crystal ordering and colloidal phase behaviour. *Adv. Colloid Interface Sci.*, *275*, 102076.